


FULL ARTICLE

Speckle contrast diffuse correlation tomography of cerebral blood flow in perinatal disease model of neonatal piglets

Chong Huang¹  | Siavash Mazdeyasna¹ | Mehrana Mohtasebi¹ | Kathryn E. Saatman² | Qiang Cheng³ | Guoqiang Yu^{1*} | Lei Chen^{2*}

¹Department of Biomedical Engineering, University of Kentucky, Lexington, Kentucky

²Department of Physiology, Spinal Cord and Brain Injury Research Center, University of Kentucky, Lexington, Kentucky

³Division of Biomedical Informatics, Department of Internal Medicine, University of Kentucky, Lexington, Kentucky

*Correspondence

Guoqiang Yu, Department of Biomedical Engineering, University of Kentucky, Lexington, KY 40506.
Email: guoqiang.yu@uky.edu

Lei Chen, Department of Physiology, Spinal Cord and Brain Injury Research Center, University of Kentucky, Lexington, KY 40536.
Email: lei.chen@uky.edu

Funding information

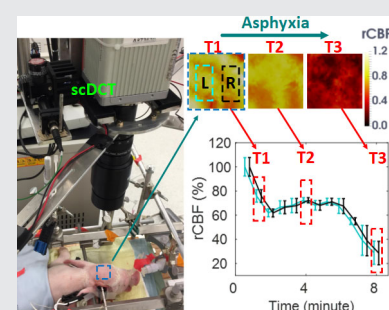
American Heart Association, Grant/Award Numbers: #14SDG20480186, #16GRNT30820006; National Institutes of Health, Grant/Award Numbers: COBRE #1P20GM121327, R01-EB028792, R01-HD101508-01, R21-AG046762, R21-HD091118, R21-NS114771; National Science Foundation, Grant/Award Number: #1539068; University of Kentucky Neuroscience Research Priority Area (NRPA) Pilot Grant

Abstract

We adapted and tested an innovative non-contact speckle contrast diffuse correlation tomography (scDCT) system for 3D imaging of cerebral blood flow (CBF) variations in perinatal disease models utilizing neonatal piglets, which closely resemble human neonates. CBF variations were concurrently measured by the scDCT and an established diffuse correlation spectroscopy (DCS) during global ischemia, intraventricular hemorrhage, and asphyxia; significant correlations were observed. Moreover, CBF variations associated reasonably with vital pathophysiological changes. In contrast to DCS measurements of mixed signals from local scalp, skull and brain, scDCT generates 3D images of CBF distributions at prescribed depths within the head, thus enabling specific determination of regional cerebral ischemia. With further optimization and validation in animals and human neonates, scDCT has the potential to be a noninvasive imaging tool for both basic neuroscience research in laboratories and clinical applications in neonatal intensive care units.

KEYWORDS

cerebral blood flow, neonatal piglet, optical imaging, perinatal disease



1 | INTRODUCTION

Perinatal diseases pose a tremendous threat to the survival and normal development of neonates. Perinatal ischemia/asphyxia is a major cause of neonatal mortality and morbidity, occurring in 1 to 26 out of 1000 live births [1, 2]. Intraventricular hemorrhage (IVH) is a serious complication of prematurity [3, 4], occurring in ~15 million children in the world every year [5]. Infants that suffer from perinatal ischemia/asphyxia

or IVH may have neurologic impairments in a broad range of motor, cognitive, and behavioral domains [6–8], thus placing a significant burden on families and society.

Perinatal diseases affect cerebral blood flow (CBF) regulations in newborn infants. Studies using PET/CT/MRI demonstrate that perinatal ischemia/asphyxia and IVH are associated with reduced CBF in certain brain regions and that patients who clinically respond to treatments have improvements in CBF [9–14]. However, these

large neuroimaging modalities are not practical for frequent use at the bedside of clinics due to their size, cost, interference with therapy, and/or need for intravenous radioactive tracer (PET/CT). Therefore, development of portable, bedside, neuroimaging methods would allow continuous assessment of brain development in newborn infants to guide timely interventions in the neonatal intensive care unit (NICU).

Portable near-infrared/diffuse correlation spectroscopy (NIRS/DCS) and corresponding diffuse optical/correlation tomography (DOT/DCT) have been tested for continuous monitoring of cerebral hemodynamics at the bedside [15–22]. However, these technologies employ limited numbers of discrete sources and detectors, thus lacking a combination of high tempo-spatial resolution and wide field-of-view (FOV) needed to image spatially distributed brain functions. Moreover, most systems utilize a cap/helmet to hold numerous sources and detectors on the fragile head of infants for contact measurements, which poses challenges on head cap design and installation, and raises safety concerns [23, 24].

Use of a charge-coupled-device (CCD) or complementary-metal-oxide-semiconductor (CMOS) camera with thousands of 2D pixels and a continued illumination achieves fast, high-resolution brain mapping. For example, laser speckle contrast imaging (LSCI) [25–27] enables noncontact 2D mapping of CBF on superficial cortices of small rodents. However, LSCI has limited penetration depth (< 1 mm), and therefore it is inadequate for noninvasive brain imaging of large animals and human subjects.

Recent advancements in using focused-point near-infrared (NIR) illumination and CCD/CMOS detection of spatial/temporal diffuse speckle contrasts have facilitated high-density imaging of blood flow variations in relatively deep tissues (centimeters) [28–33]. These technologies, including diffuse speckle contrast analysis, speckle contrast optical tomography, and speckle contrast diffuse correlation tomography (scDCT), are inherently based on the same concept despite differences in nomenclature and technological evolution. Particularly, we have developed a fully noninvasive, noncontact, multiscale scDCT (US Patent #9861319 [34]) that enables high-density 2D mapping and 3D tomography of tissue blood flow distributions. We have preliminarily tested the scDCT for imaging blood flow distributions in tissue/head-simulating phantoms, rodent brains, and other human tissues including forearm muscles, burn wounds, and mastectomy skin flaps under various medical conditions [31, 35–37]. Very recently, we conducted a preliminary study to test two preterm infant cases in the NICU by scDCT [38]. However, no pathology can be induced in human subjects to comprehensively test the feasibility and accuracy of the device for continuous CBF imaging.

The goal of the present study was to test the feasibility of our scDCT for high-density imaging of CBF variations in neonatal piglets with perinatal diseases (i.e., transient global ischemia, IVH, and perinatal asphyxia). Small animal models (primarily rodents) have been extensively used to study cerebral pathologies and interventions [39–42]. However, results from small rodents may be difficult to translate to human infants due to substantial differences in brain development and morphology. Neonatal piglets are a better complementary model because their head size and gyrencephalic brain anatomy (Supplemental Figure 1), as well as their cerebral development and pathology after IVH or asphyxia, are analogous to human neonates [43–50]. In contrast to small rodents, larger animals such as piglets are easier to implement surgeries for mimicking pathological conditions and replicating clinical findings. This pilot preclinical study in neonatal piglets with perinatal diseases moves one more step forward towards translation of our innovative scDCT technique to NICUs for continuous monitoring and rapid management of cerebral pathologies and interventions in human neonates with perinatal diseases.

2 | MATERIALS AND METHODS

All experimental protocols were approved by the Institutional Animal Care and Use Committee (IACUC) at the University of Kentucky. Figure 1 shows the experimental setting. Perinatal diseases were induced in two neonatal piglets, including transient global ischemia, IVH, and asphyxia. As shown in Figure 1A, CBF variations were concurrently monitored by the noncontact scDCT device and a contact DCS probe throughout the experiments for comparisons. Details about conventional DCS techniques for CBF measurements are in our previous publications [51–57].

As shown in Figure 1B, some physiological parameters were also recorded continuously by commercial devices including an ICP Express Monitor (82-6634H8, Codman) for intracranial pressure (ICP) measurements and a multi-channel Respirator-Oximeter (8400, Smiths Medical) for measurements of heart rate (HR), respiration rate (RR), and arterial blood oxygen saturation (SaO_2).

2.1 | scDCT technique for 3D imaging of CBF distributions

Details about scDCT technique can be found in our recent publications [31, 35, 37]. Figure 1A shows the scDCT system for noncontact imaging of CBF distribution in a piglet. Briefly, an electrically controlled galvo-mirror (switch time: 300 μs ; GVS002, Thorlabs) delivered

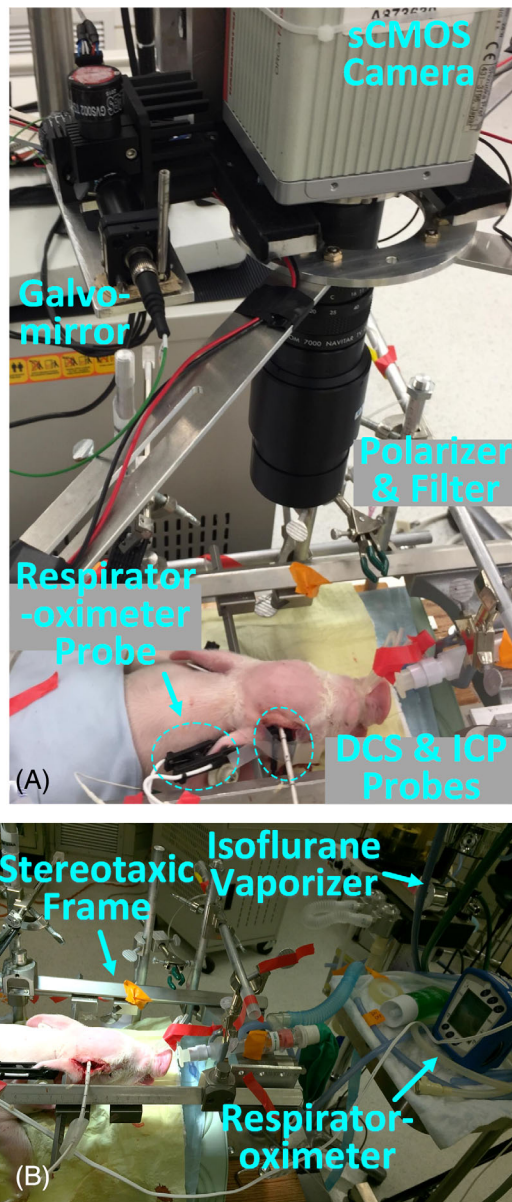


FIGURE 1 Experimental Setup for Continuous Monitoring of Neonatal Piglets with Perinatal Diseases. A, The noncontact sCDCT was used for 3D imaging of CBF distributions in piglets. DCS and ICP probes were used to record CBF and measure intracranial pressure, respectively. B, The Isoflurane anesthetized animal was secured on a stereotaxic frame with a respirator-oximeter probe clipped on the ear for continuous recording of HR, RR, and SaO_2 . CBF, cerebral blood flow; DCS, diffuse correlation spectroscopy

point NIR light (generated by a long coherence laser module: @785 nm, CrystaLaser) to multiple source positions in an adjustable region-of-interest (ROI) for deep tissue penetration. According to our simulation and measurement results, the spot diameter of sCDCT is ~ 0.3 mm. The measured power of incident light is < 0.5 mW, which meets Accessible Emission Limit (AEL) Class 3R of American National Standards Institute (ANSI) standard (< 5 mW) for safety.

A scientific CMOS (sCMOS) camera (pixels: 2048×2048 ; frame rate: 30 Hz; ORCA-Flash4.0 V3, Hamamatsu) detected spatial laser speckle contrasts resulting from motion of red blood cells (i.e., CBF) in the detected tissue volume. A zoom lens (Zoom 7000, Navitar) connected to the sCMOS camera enabled the adjustability of ROI. The f-number of the zoom lens was set up as 10 to balance Nyquist sampling criteria and adequate photon collection. All measurements in this study utilized an exposure time of 2 ms. A lever-actuated iris (SM05D5, Thorlabs) was installed in the source path to confine the light spot and intensity for adapting the dynamic range of sCOMS camera. A long-pass filter (> 750 nm, Edmund Optics) and a pair of crossed linear polarizers (LPNIRE050-B and LPNIRE200-B, Thorlabs) were utilized in the source/detector paths to block irrelevant spectra and direct reflections from sources, respectively.

In this study, 25 (5×5) source positions formed a full image circle in the selected ROI (Figure 2). Four intensity images at each source position were collected sequentially. The total sampling time for scanning over the 25 source positions was 40 seconds. After the correction of dark and shot noises in the raw intensity image taken by the sCMOS camera [31, 35], the spatial laser speckle contrast $K_s(r)$ at position r was quantified by calculating the intensity ratio of standard deviation (σ_s) and mean $\langle I \rangle$: $K_s(r) = \sigma_s / \langle I \rangle$ in a window of 7×7 pixels with an area of 0.04×0.04 mm². To improve the signal-to-noise ratio (SNR), $K_s(r)$ values were averaged over 3×3 pixel-windows (as one detector) and across 4 frames at each source position.

$K_s(r)$ is related to the normalized temporal electric field autocorrelation function $g_1(\tau, r)$ in Equation 1 [29, 31, 35]:

$$K_s(r)^2 = \frac{2\beta}{T} \int_0^T \left(1 - \frac{\tau}{T}\right) g_1^2(r, \tau) d\tau. \quad (1)$$

Where T is the camera exposure time and τ is the correlation delay time. The coherence factor β relies on light source and detection optics. For the semi-infinite geometry, we substitute the appropriate form of $g_1(r, \tau)$ into Equation 1 to obtain a nonlinear relationship between a blood flow index ($BFI(r)$) and $K_s(r)$, i.e., $K_s^2(r) = f(\alpha D_B, T, \mu_a, \mu_s', \lambda, \beta, k_0, r)$. Step-by-step derivations of this nonlinear relationship are found from Supplementary Material – Appendix A in our previous publication [35].

The combined term, αD_B , is referred to $BFI(r)$ in biological tissues and is commonly used to calculate relative changes in blood flow. D_B is the effective diffusive coefficient (cm²/s). In general, biological tissues contain both relatively static scatterers (e.g., mitochondria) and dynamic scatterers (e.g., moving red blood cells). The

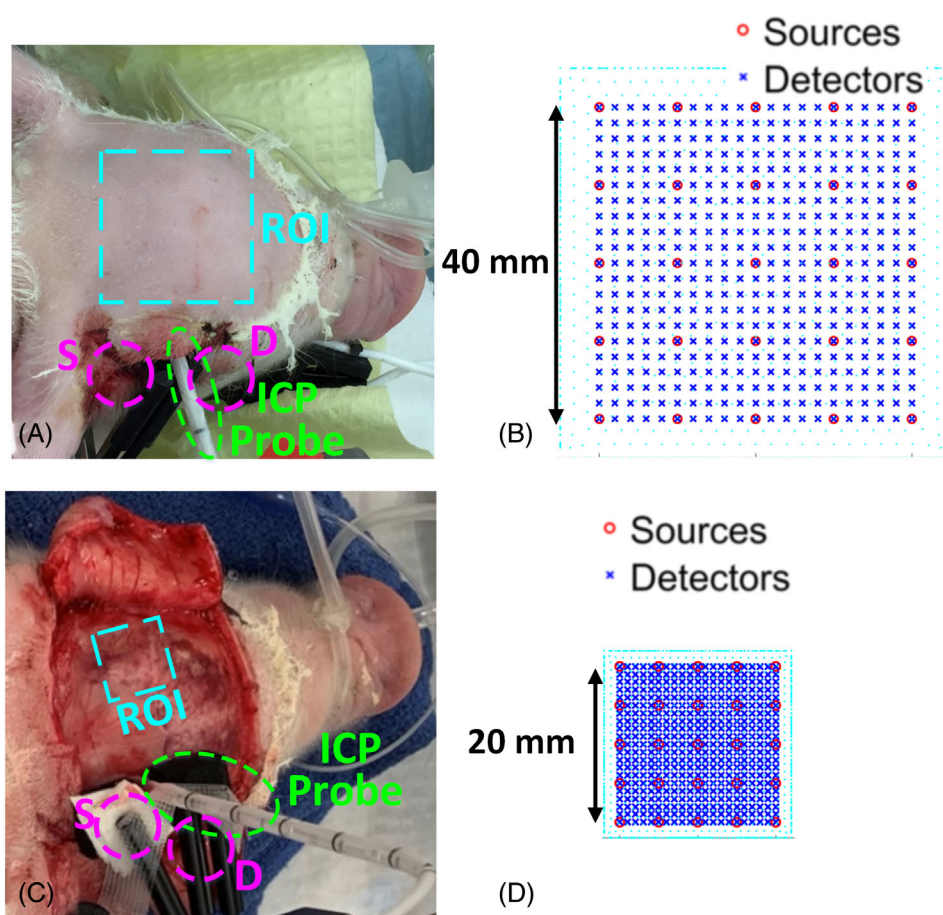


FIGURE 2 The scDCT Setup for 3D Imaging of CBF in Piglet #1 with Transient Global Ischemia, A, B, and Piglet #2 with IVH, C, D. A, An ROI of $40 \times 40 \text{ mm}^2$ was projected on the piglet head with the intact scalp for scDCT. An ICP probe was inserted into the right lateral ventricle for ICP monitoring while a conventional DCS fiber optic probe was secured next to it for CBF monitoring. B, The 5×5 sources and 21×21 detectors were distributed evenly in the $40 \times 40 \text{ mm}^2$ ROI for scDCT. C, An ROI of $20 \times 20 \text{ mm}^2$ was projected on the left skull. An ICP probe was inserted into the right lateral ventricle while a DCS fiber optic probe was secured next to it to continuously monitor CBF variations for comparisons. D, The 5×5 sources and 21×21 detectors were distributed evenly in the $20 \times 20 \text{ mm}^2$ ROI. CBF, cerebral blood flow; DCS, diffuse correlation spectroscopy

signals from static scatterers do not contribute significantly to the temporal decay of the autocorrelation function. To account for this effect, a unitless factor, α , is introduced to represent the fraction of light scattering events from dynamic scatterers. The $BFI(\mathbf{r})$ is not a measure of absolute blood flow in the strict sense. For example, $BFI(\mathbf{r})$ has a unit of cm^2/s . However, the relative change in $BFI(\mathbf{r})$ has been repeatedly shown to be a quantitative measure of relative blood flow. Particularly, it has been shown that αD_B is proportional to the absolute blood flow measured by arterial spin-labeling MRI (ASL-MRI) [58], transcranial Doppler ultrasound [59, 60], and Xenon computed tomography (Xenon-CT) [61]. In some studies, DCS has been combined with NIRS in hybrid instruments to simultaneously measure tissue blood flow and oxygenation, which allows for the derivation of metabolic rate of tissue oxygen consumption [60, 62–65].

The remaining parameters in the nonlinear function include tissue optical properties (i.e., tissue absorption coefficient $\mu_a(\mathbf{r})$ and reduced scattering coefficient $\mu'_s(\mathbf{r})$), source laser wavelength λ , and wavenumber k_0 . All parameters are known in the sense of being measured or taken from literature [35], except $BFI(\mathbf{r})$. The difference

between the measured and theoretical speckle contrasts is then minimized to obtain $BFI(\mathbf{r})$.

In total, 441 (21×21) detectors were evenly distributed between the 25 sources in the selected ROI for 3D image reconstruction. The boundary values of $BFI(\mathbf{r})$ at effective source-detector (S-D) pairs with the SNR larger than 3 were input into a modified near-infrared fluorescence and spectral tomography (NIRFAST) program for expedient finite-element-method (FEM) based tomographic reconstructions [31, 35, 55]. The node distance of the FEM mesh was set as 1 mm uniformly throughout the reconstruction volume. Due to the lack of available data regarding piglet brain properties, we assumed homogenous optical properties based on the literature for human infants: absorption coefficient $\mu_a = 0.05 \text{ cm}^{-1}$ and reduced scattering coefficient $\mu'_s = 8 \text{ cm}^{-1}$ at the wavelength of 785 nm ⁶⁷. The relative changes in CBF (rCBF) were calculated by normalizing the reconstructed $BFI(\mathbf{r})$ s at the mesh nodes to their corresponding baselines before physiological manipulations. Since all measurements in this study are continuous, β is constant and divided out in rCBF normalization. All rCBF data were smoothed using a 5-point median filter in MATLAB (Mathworks). Based on diffuse optical tomography theory [66], the

spatial resolution of scDCT was approximately 20% of the penetration depth ($\sim 1/2$ of the S-D distance).

2.2 | Animals and experimental preparations

We examined 4 birth-dead piglet carcasses to obtain anatomical data and coordinates to guide surgeries and brain hemodynamic monitoring. Supplemental Figure 1A shows skulls of a piglet (birth-dead), adult rodents (3 months), and a human infant (31 weeks after fertilization) illustrating the similarity in head sizes. Supplemental Figure 1B shows a side-view comparison between the neonatal piglet and human infant. Supplemental Figure 1C shows the gyrencephalic piglet brain.

For *in vivo* studies, two female neonatal Yorkshire piglets (postnatal day 9) were purchased from the Oak Hill Genetics and housed in a designated room for swine. Animals were kept in a warmed and ventilated animal incubator and fed with artificial swine milk every 4 hours. The piglets were fasted for at least 4 hours before surgery to avoid reflux of stomach contents. Animals were induced with 5% Isoflurane inhalation in a customized anesthesia chamber, and then intubated with a pediatric endotracheal tube (internal diameter: 3 mm) and maintained with 1.5% to 2% Isoflurane (Figure 1B). The anesthetized animal was placed prone and its head secured on a customized stereotaxic frame. Animal's body was wrapped with an electrical heated blanket under the surveillance of rectal thermometer to avoid hypothermia. A multi-channel Respirator-Oximeter sensor was clipped on the tongue (pulled out of its mouth) and ear alternately every 30 minutes (avoiding long-time compression on the same spot) to record HR, RR, and SaO_2 .

2.3 | Transient global ischemia model in Piglet #1

The transient global ischemia modeling was created in Piglet #1 through adapting our established methods used in rodents [37]. After hairs on the head and ventral cervical area were shaved with a clipper and cleaned with hair cream, the skin was sterilized with betadine and wiped with 70% Ethanol. The animal was laid supine and a 5 cm midline incision was made in the cervical area. The skin was extracted with four customized surgical hooks for better exposure of the surgical area. The underlying tissue was separated with blunt dissection until both common carotid arteries (CCAs) were exposed (Supplemental Figure 2A). A braided 6 to 0 sterile surgical suture was placed around each CCA, and a loose knot

was made on each suture without disrupting blood flow to the brain. The piglet was then laid prone. A small incision was made on the scalp above the right temporal skull, on which a small hole (3 mm in diameter) was drilled. With ultrasound imaging guidance and metal stylet assistance, an ICP probe was slowly inserted into the brain until its tip entered the right ventricle. The ICP probe position was confirmed by withdrawal of clear cerebrospinal fluid (CSF). Finally, a DCS probe with one pair of S-D fibers at the distance of 15 mm was installed next to the ICP probe (Figure 2A). The DCS probe was located >30 mm from the ROI of scDCT to avoid interference between two measurements (Figure 2C).

After a baseline measurement for 1.5 minutes, the knot on the right CCA was tightened to occlude the right CCA for ~ 7 minutes, followed by tightening the left knot for ~ 2 minutes to induce a transient global ischemia (Supplemental Figure 2B). The left and right knots were then released sequentially, allowing restoration of blood flow to the brain.

Perinatal asphyxia potentiates systemic and neurologic impairments from original diseases. After the restoration of CBF from transient global ischemia, the piglet received a hypoxic challenge before sacrifice. The inhaling gas was gradually manipulated over ~ 8 minutes from 100% O_2 /0% CO_2 to 5% O_2 /95% CO_2 through a Y-shape connector with regulatory valves [67].

Throughout experimental procedures, CBF variations were continuously monitored by the scDCT device and a custom-made DCS instrument [53, 68] for comparisons (Figure 2A). For scDCT imaging, a ROI of $40 \times 40 \text{ mm}^2$ was selected to cover both two hemispheres (Figure 2B). The effective S-D distances ranging from 7 to 19 mm were used for 3D image reconstruction [35] of rCBF distribution in a slab mesh of $50 \times 50 \times 15 \text{ mm}^3$ with total mesh nodes of 30 K. Selection of the mesh volume was based on piglet head volume (dimensions: 60 (length) \times 50 (width) \times 40 (depth) mm^3). The DCS data, sampled at 2 Hz, were normalized to the baseline to generate rCBF. DCS data were averaged at corresponding scDCT imaging periods to match data density in the time domain. Linear regression and Pearson's correlation coefficient r with 95% confidence interval (CI) were calculated to investigate correlations between the scDCT and DCS measurements. A value of $p < .05$ was considered a statistically significant correlation between the two measurements.

2.4 | IVH model in Piglet #2

IVH was induced in Piglet #2 following previously established methods [43, 45, 69, 70]. Briefly, the piglet's

scalp was sterilized with betadine and wiped with 70% Ethanol, followed by a 40-mm midline incision to expose the skull (Figure 2C). A 3-mm hole was drilled on the right frontal bone (L: 22 mm and P: -5 mm from bregma), through which the ICP probe was inserted until its tip entered the right lateral ventricle, confirmed by withdrawal of clear CSF. The baseline ICP reading was 1 to 2 mmHg. A DCS probe with one pair of S-D fibers at the distance of 15 mm was installed next to the ICP probe. The piglet was stabilized for 30 minutes. Then 1-ml heparinized autologous blood was gradually injected through the ICP probe catheter over 5 minutes to simulate IVH, followed by intermittent saline injections of

total 6 mL in ~60 minutes to keep the ICP elevated to ~4 mmHg above its baseline. After a 30-minute recovery from the IVH (i.e., ICP returned to 1–2 mmHg), Piglet #2 received the same hypoxic challenge (via manipulating gas inhalation) as Piglet #1 before euthanasia (see Section 2.3).

CBF variations were continuously monitored by scDCT and DCS (Figure 2C) before and during the blood and saline injections for ~32 minutes in total. For scDCT imaging, an ROI of $20 \times 20 \text{ mm}^2$ was selected to cover the left hemisphere (Figure 2D). The effective S-D distances ranging from 5 to 15 mm were used for 3D image reconstruction of CBF distribution in a slab mesh of

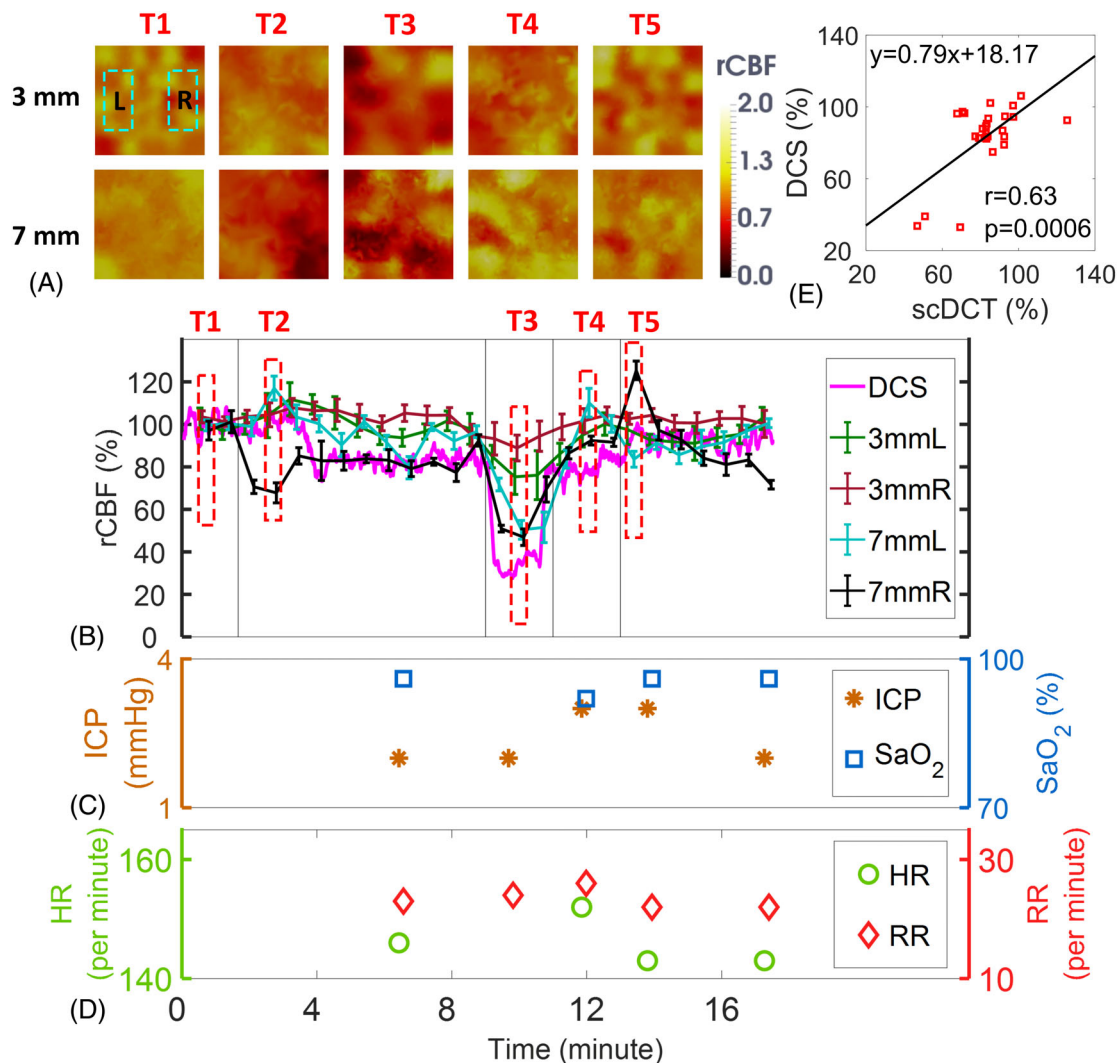


FIGURE 3 Measurement Results from Piglet #1 during Global Ischemia. A, Cross sectional views of 3D images of CBF at depths of 3 mm (scalp/skull) and 7 mm (cortex). Two regions of $20 \times 10 \text{ mm}^2$ were used to average CBF values in left and right hemispheres and marked with two dashed rectangles, respectively. T1: Baseline; T2: Right CCA ligation; T3: Bilateral ligation; T4: Releasing left ligation; T5: Releasing both ligations & recovery. B, Time-course of rCBF changes were measured concurrently by the scDCT and DCS. The dashed boxes represent the time points (T1 to T5) to take these images in Figure 3A. Error bars represent standard deviations of spatial rCBF values in the selected region. C, and D, Time-course of changes in ICP, SaO_2 , HR and RR. E, The linear regression between the scDCT and DCS measurements of rCBF in the cortex. CBF, cerebral blood flow; DCS, diffuse correlation spectroscopy

$24 \times 24 \times 15 \text{ mm}^3$ with total mesh nodes of 8 K. DCS data were sampled continuously at 2 Hz.

At the end of the experiments, both piglets were euthanatized with pentobarbital overdose, and their brains were harvested after transcardiac perfusion of heparinized saline and 4% paraformaldehyde. The brains were fixed overnight at 4°C and then sliced into coronal sections at a thickness of 5 mm.

3 | RESULTS

3.1 | Piglet #1 with transient global ischemia and hypoxic challenge

Figure 3A shows the transverse cross-sectional views of 3D images generated by scDCT at the depth of 3 mm and 7 mm beneath the intact scalp during the transient global ischemia induced by unilateral and bilateral CCA ligations. Based on the piglet head anatomy, the depth of 3 mm detects the skull/scalp whereas the depth of 7 mm reaches the brain cortex. Figure 3B shows the time-course of changes in rCBF detected concurrently by the scDCT and DCS during transient global ischemia. The sequential right and bilateral CCA ligations resulted in larger rCBF reductions in the brain cortex layer (7 mm depth) of corresponding hemispheres than those in the shallow scalp/skull layer (3 mm depth), illustrating the ability of scDCT to differentiate superficial and brain parenchyma flow variations. During right CCA occlusion (T2), rCBF in the cortex declined, reaching $67 \pm 5\%$ (mean \pm standard deviation, representing the spatial variation in the selected region and depth of 3D reconstructed rCBF values) of the baseline (T1) in the right hemisphere before further decreasing during bilateral ligations (T3) to $46 \pm 4\%$ and $50 \pm 4\%$ in right and left hemispheres, respectively. After sequentially releasing the right ligation (T4) and left ligation (T5), immediate, but transient reactive hyperemic responses in the cortex were detected in corresponding hemispheres (rCBF: $125 \pm 4\%$ in right hemisphere and $110 \pm 7\%$ in left hemisphere).

The DCS probe positioned at the right hemisphere revealed similar temporal changes in rCBF as measured by scDCT, detecting a maximal depression during bilateral ligations (Figure 3B). A significant correlation (Figure 3E) was observed between the scDCT and DCS measurements of rCBF changes in the cortex of the right hemisphere ($r = 0.63$, 95% CI = $[0.32 \text{ } 0.82]$, $p = .0006$).

Figure 3C and Figure 3D show fluctuations of ICP, SaO_2 , HR, and RR during transient global ischemia by manual recordings. Among these four measured parameters, ICP and HR varied considerably. As expected, the

release of CCA ligations resulted in transient increases of rCBF (hyperemia), thus leading to increased blood volume and pressure in the cranial cavity, evidenced by the ICP elevation (from T3 to T5).

Figure 4A shows the transverse cross-sectional views of 3D images generated by scDCT at the depths of 3 mm and 7 mm during asphyxia. Figure 4B shows the time-course of changes in rCBF detected continuously by scDCT and DCS during asphyxia. The minimum rCBF values at the end of measurement (T3) were $29 \pm 10\%$ and $30 \pm 10\%$ in left and right hemispheres of the cortex, respectively. The minimum relative blood flow values at T3 were $29 \pm 10\%$ and $29 \pm 10\%$ in left and right hemispheres of the scalp/skull, respectively. The DCS probe placed above the right temporal cortex detected declining rCBF, reaching a nadir of 15% at the end of measurements (Figure 4B). A significant correlation (Figure 4E) was observed between the scDCT and DCS measurements in the cortex ($r = 0.88$, 95% CI = $[0.62 \text{ } 0.97]$, $p = .0002$).

Figure 4C and Figure 4D show manual recordings of ICP, SaO_2 , HR, and RR during asphyxia. Asphyxia was induced by gradually increasing the concentration of CO_2 from 0% to 95% in the inhalation gas. The increased CO_2 concentration along with the reduced O_2 concentration inhibited respiratory and cardiac functions, thus leading to large drops in rCBF, ICP, SaO_2 , and HR. These physiological variations resulting from the hypoxic challenge agreed with the pathophysiological processes.

Animals were euthanatized at 3 hours after asphyxia. Acute brain autopsy revealed no overt gross anatomic changes such as brain edema, hemorrhage, and deformation.

3.2 | Piglet #2 with IVH and hypoxic challenge

Figure 5A shows the transverse cross-sectional views of 3D images reconstructed with scDCT data at the depths of 1 mm and 5 mm before, during IVH and at end of IVH measurement. Based on the anatomy of piglet head without scalp, the depth of 5 mm beneath the skull reaches the brain cortex whereas the depth of 1 mm detects the skull. Figure 5B shows the time-course of changes in rCBF detected concurrently by the scDCT and DCS during IVH. rCBF and relative blood flow reached the lowest values of $73 \pm 2\%$ in the cortex (5 mm depth) and $87 \pm 3\%$ in the skull (1 mm depth) at the end of measurements (T3). The DCS probe at the right hemisphere also detected a similar reduction over time of rCBF, which eventually reached the lowest rCBF value of 71% at the end of measurement (Figure 5B). DCS data (2 Hz

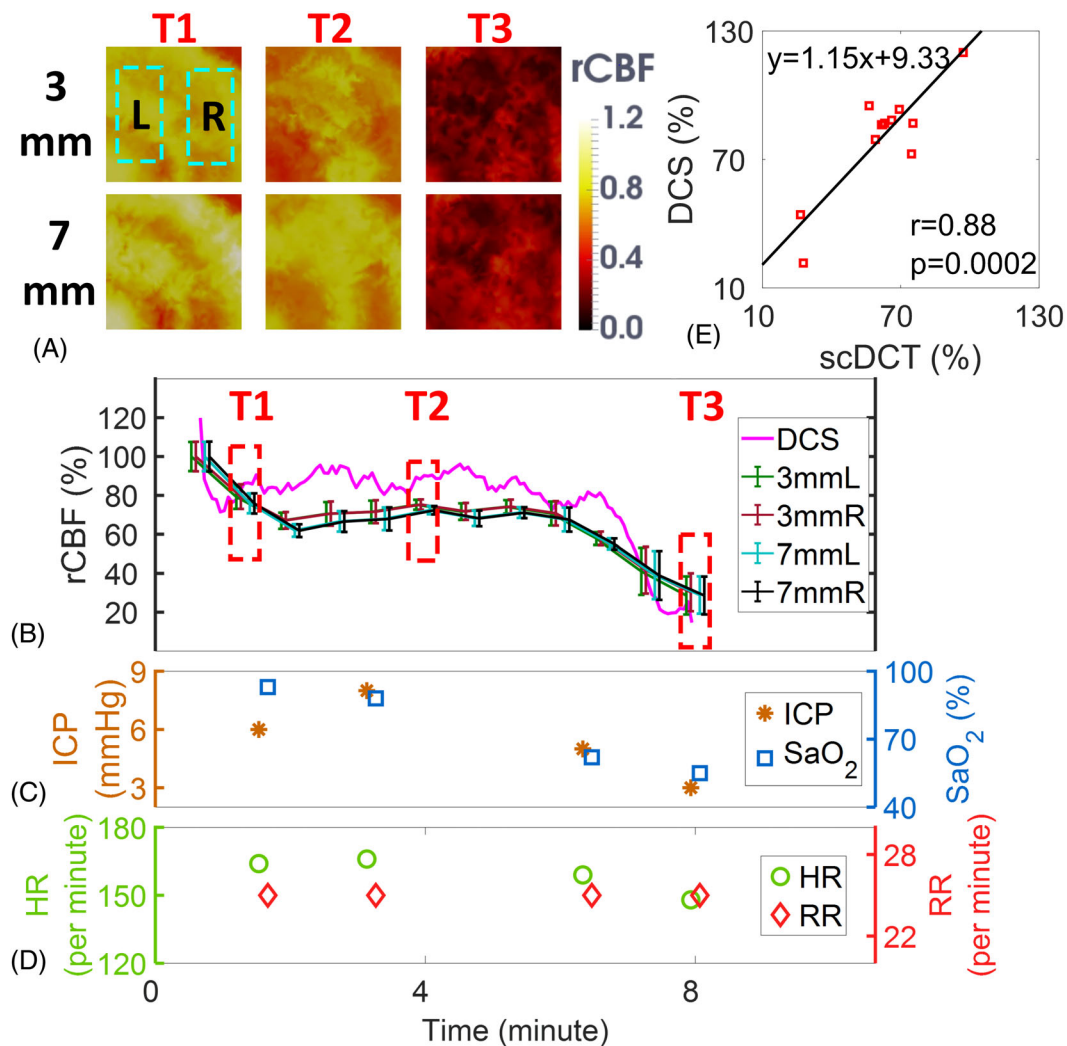


FIGURE 4 Measurement Results from Piglet #1 during Asphyxia. A, Cross sectional views of 3D images of CBF at depths of 3 mm (scalp/skull) and 7 mm (cortex). Two regions of $20 \times 10 \text{ mm}^2$ were used to average CBF values in left and right hemispheres and marked with two dashed rectangles, respectively. T1: Baseline before asphyxia; T2: During asphyxia; T3: End of measurement. B, Time-course of rCBF changes measured by the scDCT and DCS. The dashed boxes represent the time points (T1 to T3) to take these images in Figure 4A. Error bars represent standard deviations of spatial rCBF values in the selected region. C, and D, Time-course of changes in ICP, SaO_2 , HR and RR. E, The linear regression between the scDCT and DCS measurements of rCBF in the cortex. CBF, cerebral blood flow; DCS, diffuse correlation spectroscopy

sampling rate) in this subject showed large variations/oscillations, likely due to the periodic intraventricular saline injections indicated by the green triangles in Figure 5B and competitive effects from sympathetic nervous system activation. By contrast, scDCT data did not show large variations, likely due to its low sampling rate (40 seconds per image) with spatial data averaging. Nevertheless, a significant correlation (Figure 5E) was observed between the scDCT and DCS measurements in the brain cortex ($r = 0.63$, 95% CI = [0.42 0.78], $p < 10^{-5}$).

Figure 5C and Figure 5D show manual recordings of ICP, SaO_2 , HR, and RR during IVH. The ICP was elevated by the intra-ventricular injection of autologous

blood (from T1 to T2), and then maintained high by the intra-ventricular saline infusion (from T2 to T3). The HR followed the trend of ICP variation, which was likely due to sympathetic nerve activation. The RR decreased during IVH (from T1 to T3), which might be attributed to compression of the brain stem respiratory center resulting from herniation of the brainstem in response to increased ICP.

Figure 6A shows the transverse cross-sectional views of 3D images generated by scDCT at the depths of 1 mm and 5 mm during asphyxia. Figure 6B shows the time-course of changes of rCBF detected concurrently by scDCT and DCS during asphyxia. rCBF and relative blood flow reached the lowest values of $49 \pm 2\%$ in the

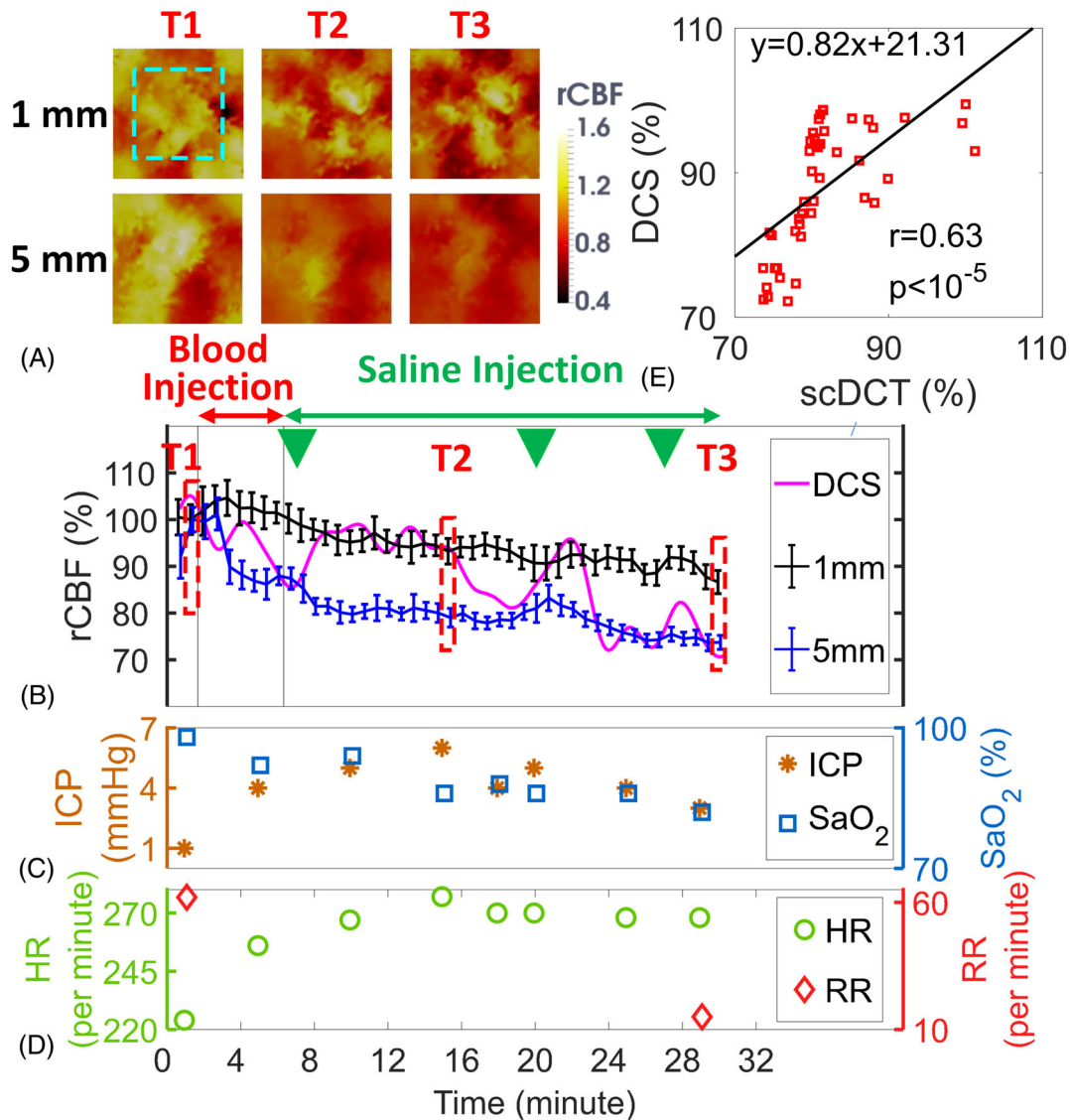


FIGURE 5 Measurement Results from Piglet #2 during IVH. A, Cross sectional views of 3D images of CBF at depths of 1 mm (skull) and 5 mm (cortex). The region of $15 \times 15 \text{ mm}^2$ used to average CBF values is marked with the dashed rectangle. T1: Baseline before IVH; T2: During IVH; T3: End of measurement. B, Time-course of rCBF changes measured by the scDCT and DCS. The dashed boxes represent the time points (T1 to T3) to take these images in Figure 5A. The green triangles represent the time points for saline injections. Error bars represent standard deviations of spatial rCBF values in the selected region. C and D Time-course of changes in ICP, SaO_2 , HR and RR. E, The linear regression between the scDCT and DCS measurements of rCBF in the cortex. CBF, cerebral blood flow; DCS, diffuse correlation spectroscopy

cortex and $75 \pm 2\%$ in the skull at the end of measurement (T3). The DCS probe at right hemisphere detected a similar decline in rCBF to a minimum of 46% at the end of asphyxia (Figure 6B). A significant correlation (Figure 6E) was observed between the scDCT and DCS measurements in the brain cortex ($r = 0.77$, 95% CI = [0.47 0.91], $p = .0002$).

Figure 6C and Figure 6D show manual recordings of ICP, SaO_2 , and HR during asphyxia. Note that the Respirometer accidentally did not report RR properly during this session, possibly from the hypoxia-induced changes of breath

pattern and air flow. ICP, SaO_2 , and HR decreased continuously along with rCBF reduction during asphyxia, indicating the impact of hypoxic stress on the brain.

Figure 7A shows sliced coronal sections with 5 mm thickness of the piglet brain after IVH. The injected autologous blood was mostly found in the ipsilateral lateral ventricle, with additional blood localized to the 3rd and 4th ventricles. Figure 7B shows the enlarged lateral ventricle with blood clot and the deflected midline, which are consistent with the findings from the ultrasound image (Figure 7C).

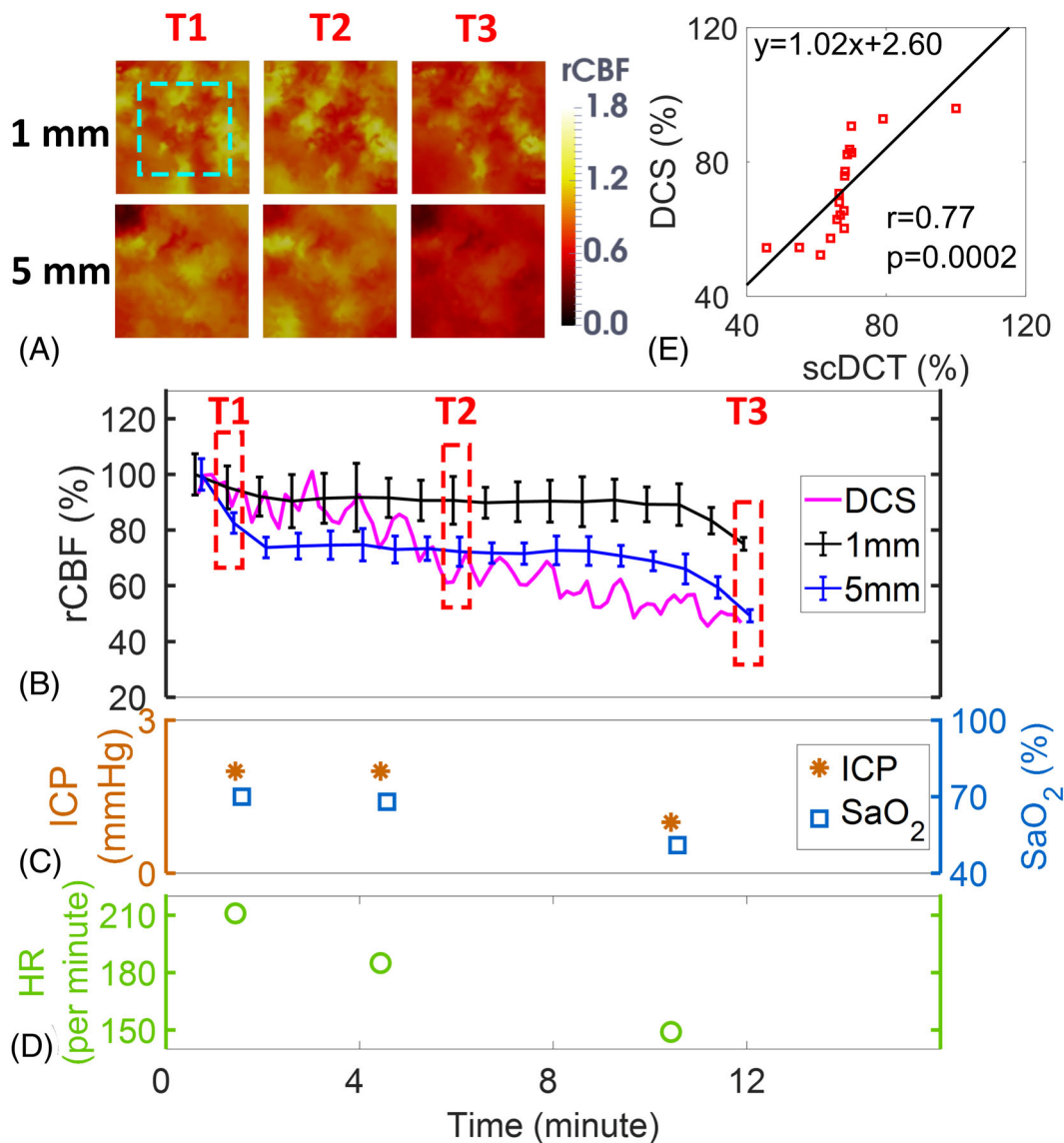


FIGURE 6 Measurement Results from Piglet #2 during Asphyxia. A, Cross sectional views of 3D images of CBF at depths of 1 mm (skull) and 5 mm (cortex). The region of $15 \times 15 \text{ mm}^2$ used to average CBF values is marked with the dashed rectangle. T1: Baseline before asphyxia; T2: During asphyxia; T3: End of measurement. B, Time-course of rCBF changes measured by the scDCT and DCS. The dashed boxes represent the time points (T1 to T3) to take these images in Figure 6A. Error bars represent standard deviations of spatial rCBF values in the selected region. C and D, Time-course of changes in ICP, SaO_2 , and HR. E, The linear regression correlation between the scDCT and DCS measurements of rCBF changes in the cortex. CBF, cerebral blood flow; DCS, diffuse correlation spectroscopy

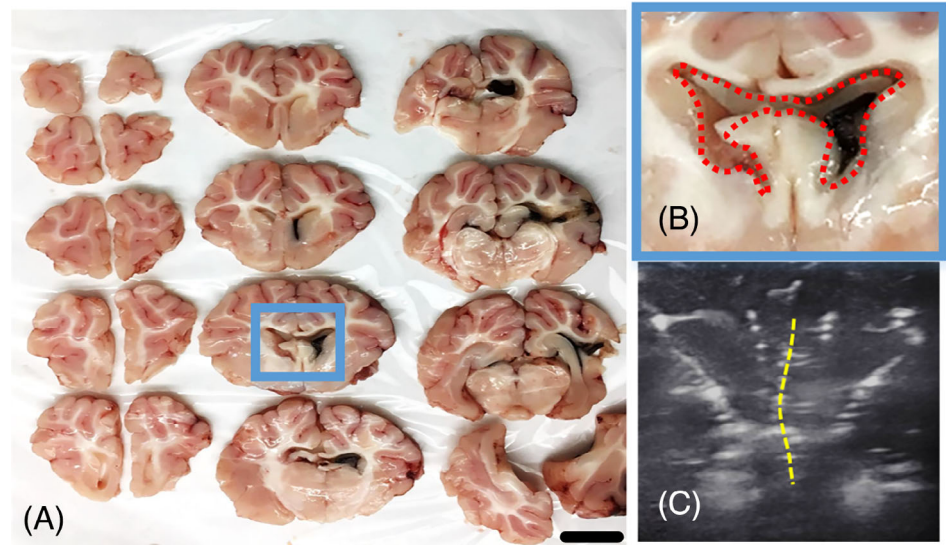
4 | DISCUSSION AND CONCLUSIONS

4.1 | Study motivation and innovation

Newborn infants who experience perinatal asphyxia or preterm birth are at high risk of cerebral hemodynamic instability, which is often associated with brain injury. Currently, there is no established bedside method to continuously monitor cerebral hemodynamics in the NICU for timely diagnosis and day-to-day management. Our innovative scDCT enables noninvasive and noncontact

imaging of CBF in neonatal brains with high sampling density and flexible ROI. The scDCT scans focused point NIR light for deep tissue penetration and collects high-density images with a 2D camera. The rapid high-density sampling improves tempo-spatial resolution and SNRs (via spatially averaging multiple pixel windows). Moreover, scDCT allows customization of the ROI for imaging different tissues/organs with varied scales/dimensions. We have recently demonstrated the feasibility of scDCT for 3D imaging of blood flow distributions in rodent brains [37], and in human wounds [71] and reconstructive skin flaps [35, 36].

FIGURE 7 IVH pathology in Piglet #2. A and B Blood clots, a histological characteristic of IVH, are visualized in ipsilateral lateral ventricle and 3rd ventricle. C, The ventriculomegaly and midline shift (yellow dotted line) shown in the ultrasound image. Scale bar: 1 cm. IVH, intraventricular hemorrhage



This preclinical study was designed to adapt and test the scDCT for high-density imaging of CBF variations in neonatal piglets with perinatal diseases (transient global ischemia, IVH, and perinatal asphyxia). We created perinatal disease models in neonatal piglets as they closely resemble human neonates in terms of body and head sizes, techniques utilized for supporting and monitoring, and pathological measurements (see Supplemental Figure 1 and Figure 7). Indeed, our vital surveillance and pathological outcomes from these models reflected clinical observations and characteristics of the diseases (Figures 3-7), thus offering a research platform to optimize the innovative scDCT for future translational applications in human subjects with perinatal diseases.

4.2 | Comparisons with the established DCS technique

Measurements of rCBF obtained by scDCT were compared to concurrent measurements using the well-established DCS approach. On the whole, the two approaches revealed similar patterns and magnitude of rCBF changes in response to several distinct neurological challenges, including global ischemia, asphyxia and IVH. In fact, statistically significant correlations between the two measurements were observed (Figures 3E-6E), indicating the capability of scDCT for transcranial brain imaging.

Although rCBF responses measured by scDCT generally tracked those detected using DCS, some discrepancies were observed (Figures 3B-6B) which may be related to differences inherent in these methodologies. scDCT uses a CMOS/CCD camera for 2D detection to measure the *spatial fluctuation* of diffuse speckle contrast K_s with

an exposure time of a few milliseconds. In contrast, DCS uses a high-speed, single-photon-counting avalanche photodiode for 1D detection to measure the *temporal fluctuation* of diffuse speckle contrast, which is typically on the order of tens to hundreds of milliseconds. In addition, compared to the DCS with a sampling time of 0.5 seconds, the scDCT has a much longer scanning time of 40 seconds, leading to averaging effects on scDCT images. Although measurements were obtained concurrently, the scDCT light power (<0.5 mW, measured by a power meter) is much lower than the DCS light power (>10 mW) and should not affect DCS measurements at a relatively long distance of 30 mm (Figure 2C). Indeed, no obvious differences were observed in DCS raw data obtained when the scDCT light was on versus off (data not shown).

Conventional DCS employs a fiber-optic probe in contact with the head for spectroscopic (not tomographic) measurements of rCBF. One pair of S-D fibers at the distance of 15 mm was used in our DCS probe, allowing detection of CBF at depths of up to ~8 mm (~1/2 of S-D distance) [51, 53]. However, it is important to note that DCS measures mixed signals of rCBF from the scalp, skull and brain. In contrast, scDCT generates 3D images of rCBF distributions at different depths, thus allowing correction of partial volume effects by the overlaying scalp/skull tissues. As a result, larger rCBF changes were detected by scDCT in the cortex than the shallow scalp/skull in the experiments that impacted layered tissues differently (Figures 3B, 5B, 6B). Finally, differences in anatomical location and tissue volumes sampled by scDCT and DCS, necessitated by separating the two probes to avoid physical conflict and optical interference (Figure 2), may have contributed to differences in rCBF changes detected by the two approaches. Comparisons of

scDCT with 3D imaging modalities (e.g., using the ASL-MRI as a predicate modality) are needed to further validate the accuracy of scDCT in resolving spatial differences in rCBF.

4.3 | Interpretation of rCBF responses in piglets

Piglet #1: Global Ischemia Modeling. The scDCT measurements showed that the sequential CCA ligations induced cerebral ischemia first in the ipsilateral hemisphere and then bilaterally. Brain perfusion relies mostly on blood supplies by left and right CCAs, while scalp and skull receive collateral blood flow from vertebral artery and basilar artery. Moreover, the neonatal skull is still filled with cranial bone marrow that has enriched microcirculation but relatively slower blood flow. In addition, neonatal scalp has less density of blood vessels compared to the brain. Taken together, scalp and skull were less impacted by the transient CCA ligations than the brain (Figure 3A and Figure 3B). As expected, rCBF recovered gradually towards its baseline after releasing the ligations.

During asphyxia, however, the animal suffered systemic hypoxic stress and depressed cardiac function. Therefore, rCBF and relative blood flow continuously decreased to $25 \pm 11\%$ and $33 \pm 12\%$ in the cortex and top scalp/skull, respectively (Figure 4A and Figure 4B), suggesting its global impact on blood flow in all tissue layers.

Piglet #2: IVH Modeling. ICP elevations (Figure 5C) along with other characteristic features of IVH, including blood clots in the lateral ventricle and ventriculomegaly (Figure 7), indicated the success in establishing the piglet model of IVH.

IVH resulted in gradual reductions in blood flow and led to the lowest values of $73 \pm 2\%$ and $87 \pm 3\%$ at the brain cortex and superficial skull layer, respectively (Figure 5A and Figure 5B). During asphyxia, blood flow decreased continuously to $49 \pm 2\%$ and $75 \pm 2\%$ in the cortex and skull, respectively (Figure 6A and Figure 6B). blood flow reductions were much higher in the cortex than in the skull, as the IVH and asphyxia mostly impacted the cortex with higher blood perfusion compared to that of the skull.

rCBF response discrepancies during asphyxia between the two piglets. In addition to individual heterogeneous responses, the discrepancy in rCBF responses to asphyxia between the two piglets (Figure 4 and Figure 6) was likely due to the influence of the scalp and differences in pathological stresses. Piglet #1 had an intact scalp with a transient global ischemic challenge that

allows CBF restoration, whereas Piglet #2 had an exposed skull with scalp retraction to induce IVH that leads to CBF depression. The scalp has higher blood flow than the skull and is more susceptible to global ischemia/hypoxia. As such, Piglet #1 with global ischemia (Figure 4) showed more synchronous decreases of rCBF in both layers than Piglet #2 with IVH (Figure 6).

4.4 | Study challenges, limitations, and perspectives

We recognize challenges and limitations of this pilot study. One major limitation is the small number of animals ($n = 2$), which precludes any statements related to the variation across animals in physiological responses to induction of cerebral ischemia, IVH or hypoxia. Another limitation is the lack of continuous and automatic recording of vital signals, such as ICP, SaO_2 , HR, and RR. Also, this acute nonsurvival study should be extended to a long-term survival study to longitudinally monitor CBF variations along with the progress of brain pathologies. Moreover, scDCT yielded only relative CBF variations. Nonetheless, we believe this pilot study in large animal models (piglets) with timely technology development is an important step towards future studies that would enroll more animals with more extensive measurements to further validate the innovative scDCT technique against gold standards for absolute CBF measurements.

There are also technological challenges to be overcome. While constant optical properties ($\mu_a(\mathbf{r})$ and $\mu'_s(\mathbf{r})$) were assumed from the literature [72], they may vary across different tissue layers and between animals. Also, using a homogenous mesh with assumed optical properties to represent a head with layered tissues (scalp/skull and brain) may result in reconstruction errors. Although beyond the scope of this study, we may adapt a layered mesh with measured optical properties and cerebral oxygenation using NIRS or multiple-wavelength scDCT in the future to improve image reconstruction [73–75]. Moreover, simultaneous measurements of both CBF and cerebral oxygenation allow the derivation of cerebral oxidative metabolism [60, 63, 65], another important parameter for brain function assessment.

The limiting factors for temporal resolution of scDCT include the number of source positions over the ROI and SNR. In this study, 25 (5×5) source positions formed a full image circle in the selected ROI. Four intensity images at each source position were collected sequentially for averaging to improve the SNR. Therefore, the total sampling time for scanning over the 25 source positions was 40 seconds. While decreasing the number of source positions and number of images at each source

position would improve the temporal resolution, this would reduce the sampling density and SNR. Alternatively, we may implement a new reconstruction scheme based on a moving window, where a tomographic image is obtained as data from a new source position becomes available [76]. As a result, the sampling time can be shortened tens of folds (e.g., 1.6 seconds = 40 seconds/25 sources).

Traditional FEM-based reconstruction takes minutes to hours depending on size of mesh nodes [52, 54, 55]. New FEM-based frameworks collectively utilize parallelization of fluence and Jacobian calculations across S-D pairs and a reduced sensitivity matrix for rapid image reconstruction in near real-time [77]. We expect to eventually adapt these fast sampling schemes and reconstruction methodologies to achieve near real-time cerebral imaging.

The ICP and vitals (SaO₂, HR, and RR) were continuously monitored by an ICP Express device and a Respirator-Oximeter, respectively. Their outputs were recorded manually and intermittently, with missing data due to failures of reporting from these devices. In the future, we may develop a computer-controlled interface to automatically read the outputs from the two devices and synchronize them with scDCT measurements.

In addition to this preclinical study, our scDCT has been tested for noninvasive imaging of human preterm brains [38] and human mastectomy skin flaps [36, 78, 79] with a penetration depth of ~10 mm. This depth (10 mm) enables penetrating deeply into human infant brains [38]. We are currently optimizing the system (e.g., wavelengths/powers of laser diodes and sensitivities of cameras) to penetrate deeper with the goal of imaging human adult brains.

5 | CONCLUSIONS

This pilot study adapted and tested our innovative scDCT system for 3D imaging of CBF variations in neonatal piglets, which closely resembled human neonates in terms of head anatomy and brain pathology. Perinatal diseases including transient global ischemia, IVH, and asphyxia were induced in two neonatal piglets. CBF variations were concurrently monitored by our noncontact scDCT imaging device and a contact DCS probe throughout all experiments for comparisons. Significant correlations were observed between the scDCT and DCS measurements in the brain cortex. Moreover, CBF variations during perinatal disease processes associated reasonably with vital pathophysiological changes (e.g., ICP, SaO₂, HR, and RR). In contrast to the DCS measurements of mixed signals from local scalp/skull and brain, scDCT generates 3D images of rCBF distributions at different

depths over a large ROI/FOV, thus enabling correction of partial volume effects by the overlaying scalp/skull tissues. Moreover, high-density sampling in a large ROI/FOV by the scDCT enabled determination of regional ischemia in the brain. With further optimization and validation in animals and human neonates against gold standards, we expect that the scDCT will become a valuable noninvasive imaging tool for both basic neuroscience researches in laboratories and clinical applications in NICUs to evaluate various cerebral pathological conditions and interventions.

ACKNOWLEDGMENT

This work was supported by the National Institutes of Health (NIH, R01-HD101508-01, R01-EB028792, R21-HD091118, R21-AG046762, R21-NS114771 and COBRE #1P20GM 121327), American Heart Association (AHA #16GRNT 30820006 and #14SDG20480186), National Science Foundation (NSF #1539068), and a University of Kentucky Neuroscience Research Priority Area (NRPA) Pilot Grant. The content is solely the responsibility of the authors and does not necessarily represent the official views of the NIH, AHA, NSF, or NRPA.

DATA AVAILABILITY STATEMENT

The data that support the findings of this study are available from the corresponding author upon reasonable request.

ORCID

Chong Huang  <https://orcid.org/0000-0002-5260-9112>

REFERENCES

- [1] N. N. Finer, C. M. Robertson, R. T. Richards, L. E. Pinnell, K. L. Peters, *J. Pediatr.* **1981**, 98, 112.
- [2] A. Lorek, Y. Takei, E. B. Cady, J. S. Wyatt, J. Penrice, A. D. Edwards, D. Peebles, M. Wylezinska, H. Owen-Reece, V. Kirkbride, C. E. Cooper, R. F. Aldridge, S. C. Roth, G. Brown, D. T. Delpy, E. O. R. Reynolds, *Pediatr. Res.* **1994**, 36, 699.
- [3] A. Mukerji, V. Shah, P. S. Shah, *Pediatrics.* **2015**, 136, 1132.
- [4] N. Younge, R. F. Goldstein, C. M. Bann, S. R. Hintz, R. M. Patel, P. B. Smith, E. F. Bell, M. A. Rysavy, A. F. Duncan, B. R. Vohr, A. Das, R. N. Goldberg, R. D. Higgins, C. M. Cotten, *The New England J. Med.* **2017**, 376, 617.
- [5] H. Blencowe, S. Cousens, D. Chou, M. Oestergaard, L. Say, A. B. Moller, M. Kinney, J. Lawn, *Reprod. Health.* **2013**, 10 (Suppl 1), S2.
- [6] S. Shankaran, A. Pappas, S. A. McDonald, B. R. Vohr, S. R. Hintz, K. Yolton, K. E. Gustafson, T. M. Leach, C. Green, R. Bara, C. M. Petrie Huitema, R. A. Ehrenkranz, J. E. Tyson, A. Das, J. Hammond, M. Peralta-Carcelen, P. W. Evans, R. J. Heyne, D. E. Wilson-Costello, Y. E. Vaucher, C. R. Bauer, A. M. Dusick, I. Adams-Chapman, R. F. Goldstein, R. Guillet, L. A. Papile, R. D. Higgins, N. N. R. N. Eunice Kennedy, *N. Engl. J. Med.* **2012**, 366, 2085.

- [7] M. van Handel, H. Swaab, L. S. de Vries, M. J. Jongmans, *J. Pediatr. Psychol.* **2010**, 35, 286.
- [8] M. van Handel, H. Swaab, L. S. de Vries, M. J. Jongmans, *Eur J Pediatr* **2007**, 166, 645.
- [9] D. Ziegelitz, J. Arvidsson, P. Hellstrom, M. Tullberg, C. Wikkelso, G. Starck, *J. Cereb. Blood Flow Metab.* **2016**, 36, 1755.
- [10] J. J. Volpe, P. Herscovitch, J. M. Perlman, M. E. Raichle, *Pediatrics*. **1983**, 72, 589.
- [11] L. R. Ment, R. A. Ehrenkranz, R. C. Lange, P. T. Rothstein, C. C. Duncan, *Pediatrics*. **1981**, 68, 763.
- [12] M. Proisy, I. Corouge, A. Legouhy, A. Nicolas, V. Charon, N. Mazille, S. Leroux, B. Bruneau, C. Barillot, J. C. Ferre, *Neuroimage Clin.* **2019**, 24, 101939.
- [13] R. E. Giesinger, L. J. Bailey, P. Deshpande, P. J. McNamara, *J Pediatr.* **2017**, 180, 22.
- [14] D. Tortora, F. M. Lo Russo, M. Severino, A. Parodi, P. Massirio, L. A. Ramenghi, A. Rossi, *Neuroradiology* **2020**, 62, 1689.
- [15] E. M. W. Kooi, E. A. Verhagen, J. W. J. Elting, M. Czosnyka, T. Austin, F. Y. Wong, M. J. H. Aries, *Expert Rev Neurotherapeutics*. **2017**, 17, 801.
- [16] G. Greisen, B. Andresen, A. M. Plomgaard, S. Hyttel-Sorensen, *Neurophotonics*. **2016**, 3, 31407.
- [17] J. Banerjee, T. S. Leung, N. Aladangady, *Early Hum. Dev.* **2016**, 97, 1.
- [18] V. Y. Chock, L. A. Rose, J. V. Mante, R. Pun, *Pediatr. Res.* **2016**, 80, 675.
- [19] M. A. Underwood, J. M. Milstein, M. P. Sherman, *Neonatology*. **2007**, 91, 134.
- [20] P. Zaramella, F. Freato, V. Quaresima, M. Ferrari, M. Bartocci, M. Rubino, E. Falcon, L. Chiangetti, *Pediatr Int.* **2006**, 48, 305.
- [21] A. M. Naidech, B. R. Bendok, M. L. Ault, T. P. Bleck, *Neurocrit Care*. **2008**, 9, 326.
- [22] E. E. Severdija, N. P. Vranken, S. Teerenstra, Y. M. Ganushchak, P. W. Weerwind, *J. Extra Corpor. Technol.* **2015**, 47, 32.
- [23] B. R. White, S. M. Liao, S. L. Ferradal, T. E. Inder, J. P. Culver, *Neuroimage*. **2012**, 59, 2529.
- [24] A. T. Eggebrecht, B. R. White, S. L. Ferradal, C. Chen, Y. Zhan, A. Z. Snyder, H. Dehghani, J. P. Culver, *Neuroimage*. **2012**, 61, 1120.
- [25] J. Senarathna, A. Rege, N. Li, N. V. Thakor, *IEEE reviews in biomedical engineering*. **2013**, 6, 99.
- [26] C. Zhou, T. Shimazu, T. Durduran, J. Luckl, D. Y. Kimberg, G. Yu, X. H. Chen, J. A. Detre, A. G. Yodh, J. H. Greenberg, *J. Cerebral Blood Flow Metabolism: Official J. Int. Soc. Cerebral Blood Flow Metabolism*. **2008**, 28, 1275.
- [27] T. Durduran, M. G. Burnett, G. Q. Yu, C. Zhou, D. Furuya, A. G. Yodh, J. A. Detre, J. H. Greenberg, *J Cerebr Blood F Met.* **2004**, 24, 518.
- [28] R. Bi, J. Dong, K. Lee, *Opt Express*. **2013**, 21, 22854.
- [29] R. Bi, J. Dong, K. Lee, *Opt. Lett.* **2013**, 38, 1401.
- [30] H. M. Varma, C. P. Valdes, A. K. Kristoffersen, J. P. Culver, T. Durduran, *Biomed. Opt. Express* **2014**, 5, 1275.
- [31] C. Huang, D. Irwin, Y. Lin, Y. Shang, L. He, W. Kong, J. Luo, G. Yu, *Med Phys.* **2015**, 42, 4000.
- [32] C. Huang, M. Seong, J. P. Morgan, S. Mazdeyasna, J. G. Kim, J. T. Hastings, G. Yu, *J Biomed Opt.* **2016**, 21, 80501.
- [33] C. Huang, Y. Gu, J. Chen, A. A. Bahrani, E. G. A. Jawdeh, H. S. Bada, K. Saatman, G. Yu, L. Chen, *Ieee J Sel Top Quant.* **2019**, 25, 1.
- [34] G. Yu, Y. Lin, C. Huang US Patent #9861319 **2016**.
- [35] C. Huang, D. Irwin, M. Zhao, Y. Shang, N. Agochukwu, L. Wong, G. Yu, *IEEE T Med Imaging*. **2017**, 36, 2068.
- [36] S. Mazdeyasna, C. Huang, M. Zhao, N. B. Agochukwu, A. A. Bahrani, L. Wong, G. Yu, *J. Biomed. Opt.* **2018**, 23, 96005.
- [37] C. Huang, S. Mazdeyasna, L. Chen, E. G. Abu Jawdeh, H. S. Bada, K. E. Saatman, L. Chen, G. Yu, *Neuroimage*. **2019**, 198, 160.
- [38] E. G. Abu Jawdeh, C. Huang, S. Mazdeyasna, L. Chen, L. Chen, H. Bada, S. G. Yu, *Phys. Med. Biol.* **2020**, 65, 245009.
- [39] M. F. Chesselet, S. T. Carmichael, *Neurotherapeutics* **2012**, 9, 241.
- [40] A. Durukan, D. Strbian, T. Tatlisumak, *Current Pharmaceutical Des.* **2008**, 14, 359.
- [41] B. Ellenbroek, J. Youn, *Dis Model Mech.* **2016**, 9, 1079.
- [42] B. Schaller, R. Graf, *J. Neurol.* **2002**, 249, 1503.
- [43] K. Aquilina, C. Hobbs, S. Cherian, A. Tucker, H. Porter, A. Whitelaw, M. Thoresen, *J. Neurosurg.* **2007**, 107, 126.
- [44] T. Tang, R. J. Sadleir, *Physiol. Meas.* **2011**, 32, 811.
- [45] T. Tang, M. D. Weiss, P. Borum, S. Turovets, D. Tucker, R. Sadleir, *Physiol. Meas.* **2016**, 37, 751.
- [46] A. Barbier, A. Boivin, W. Yoon, D. Vallerand, R. W. Platt, F. Audibert, K. J. Barrington, P. S. Shah, A. M. Nuyt, N. Canadian Neonatal, *Pediatrics* **2013**, 131, e1158.
- [47] C. Amiel-Tison, J. Gosselin, C. Infante-Rivard, *Dev Med Child Neurol* **2002**, 44, 643.
- [48] Z. Li, B. K. Park, W. Liu, J. Zhang, M. P. Reed, J. D. Rupp, C. N. Hoff, J. Hu, *Plos One* **2015**, 10, e0127322.
- [49] R. Bolander, B. Mathie, C. Bir, D. Ritzel, *Ann. Biomed. Eng.* **2011**, 39, 2550.
- [50] M. A. O'Reilly, A. Muller, K. Hynynen, *Ultrasound Med Biol* **2011**, 37, 1930.
- [51] N. B. Agochukwu, C. Huang, M. Zhao, A. A. Bahrani, P. McGrath, G. Yu, L. Wong, *Plast Reconstr Surg* **2017**, 140, 26.
- [52] C. Huang, Y. Lin, L. He, D. Irwin, M. M. Szabunio, G. Yu, *Appl. opt.* **2015**, 54, 8808.
- [53] C. Huang, J. P. Radabaugh, R. K. Aouad, Y. Lin, T. J. Gal, A. B. Patel, J. Valentino, Y. Shang, G. Yu, *J. Biomed. Opt.* **2015**, 20, 75008.
- [54] L. He, Y. Lin, C. Huang, D. Irwin, M. M. Szabunio, *J. Biomed. Opt.* **2015**, 20, 86003.
- [55] Y. Lin, C. Huang, D. Irwin, L. He, Y. Shang, G. Yu, *Appl. Phys. Lett.* **2014**, 104, 121103.
- [56] T. Li, Y. Lin, Y. Shang, L. He, C. Huang, M. Szabunio, G. Yu, *Sci. Rep.* **2013**, 3, 1358.
- [57] Y. Lin, L. He, Y. Shang, G. Yu, *J. Biomed. Opt.* **2012**, 17, 010502.
- [58] G. Yu, T. F. Floyd, T. Durduran, C. Zhou, J. Wang, J. A. Detre, A. G. Yodh, *Opt. Express* **2007**, 15, 1064.
- [59] E. M. Buckley, N. M. Cook, T. Durduran, M. N. Kim, C. Zhou, R. Choe, G. Q. Yu, S. Shultz, C. M. Sehgal, D. J. Licht, P. H. Arger, M. E. Putt, H. Hurt, A. G. Yodh, *Opt. Express* **2009**, 17, 12571.
- [60] N. Roche-Labarbe, S. A. Carp, A. Surova, M. Patel, D. A. Boas, P. E. Grant, M. A. Franceschini, *Hum. Brain Mapp.* **2010**, 31, 341.
- [61] M. N. Kim, T. Durduran, S. Frangos, B. L. Edlow, E. M. Buckley, H. E. Moss, C. Zhou, G. Yu, R. Choe, E. Maloney-Wilensky, R. L. Wolf, M. S. Grady, J. H. Greenberg, J. M.

- Levine, A. G. Yodh, J. A. Detre, W. A. Kofke, *Neurocrit Care*. **2010**, 12, 173.
- [62] P. Y. Lin, K. Hagan, A. Fenoglio, P. E. Grant, M. A. Franceschini, *Sci. Rep.* **2016**, 6, 25903.
- [63] M. Diop, J. Kishimoto, V. Toronov, D. S. Lee, K. S. Lawrence, *Biomed. Opt. Express* **2015**, 6, 3907.
- [64] T. Durduran, G. Yu, M. G. Burnett, J. A. Detre, J. H. Greenberg, J. Wang, C. Zhou, A. G. Yodh, *Opt. Lett.* **2004**, 29, 1766.
- [65] N. Roche-Labarbe, A. Fenoglio, H. Radhakrishnan, M. Kocienski-Filip, S. A. Carp, J. Dubb, D. A. Boas, P. E. Grant, M. A. Franceschini, *NeuroImage* **2014**, 85(Pt 1), 279.
- [66] I. Meglinski, *Biophotonics for Medical Applications*, Elsevier, Cambridge, England, **2015**.
- [67] M. E. Brevard, T. Q. Duong, J. A. King, C. F. Ferris, *Magnetic Resonance Imaging*. **2003**, 21, 995.
- [68] Y. Shang, Y. Zhao, R. Cheng, L. Dong, D. Irwin, G. Yu, *Opt. Lett.* **2009**, 34, 3556.
- [69] K. Aquilina, E. Chakkarapani, M. Thoresen, *J. Neurosurg. Pediatr.* **2012**, 10, 529.
- [70] R. J. Sadleir, T. Tang, A. S. Tucker, P. Borum, M. Weiss, "Detection of intraventricular blood using EIT in a neonatal piglet model," 2009 *Annual International Conference of the IEEE Engineering in Medicine and Biology Society*, Minneapolis, MN, **2009**, 3169. <https://doi.org/10.1109/IEMBS.2009.5334510>.
- [71] M. Zhao, S. Mazdeyasna, C. Huang, N. Agochukwu-Nwubah, A. Bonaroti, L. Wong, *Mil. Med.* **2020**, 185, 82.
- [72] J. Zhao, H. S. Ding, X. L. Hou, C. L. Zhou, B. Chance, *J. Biomed. Opt.* **2005**, 10, 024028.
- [73] J. Liu, H. Zhang, J. Lu, X. Ni, Z. Shen, *Biomed Opt Express*. **2017**, 8, 4537.
- [74] C. P. Valdes, H. M. Varma, A. K. Kristoffersen, T. Dragojevic, J. P. Culver, T. Durduran, *Biomed Opt Express*. **2014**, 5, 2769.
- [75] D. Tamborini, P. Farzam, B. Zimmermann, K. C. Wu, D. A. Boas, M. A. Franceschini, *Neurophotonics*. **2018**, 5, 11015.
- [76] T. Dragojevic, E. E. Vidal Rosas, J. L. Hollmann, J. P. Culver, C. Justicia, T. Durduran, *NEUROW.* **2019**, 6, 45001.
- [77] X. Wu, A. T. Eggebrecht, S. L. Ferradal, J. P. Culver, H. Dehghani, *Biomed. Opt. Express* **2015**, 6, 4567.
- [78] A. Bonaroti, R. C. DeCoster, S. Mazdeyasna, C. Huang, G. Yu, L. Wong, *Plast Reconstr Surg* **2019**, 144, 933e.
- [79] M. Zhao, S. Mazdeyasna, C. Huang, N. Agochukwu-Nwubah, A. Bonaroti, L. Wong, G. Yu, *Mil Med* **2019**, 185, 82.

SUPPORTING INFORMATION

Additional supporting information may be found online in the Supporting Information section at the end of this article.

How to cite this article: Huang C, Mazdeyasna S, Mohtasebi M, et al. Speckle contrast diffuse correlation tomography of cerebral blood flow in perinatal disease model of neonatal piglets. *J. Biophotonics*. 2021;e202000366. <https://doi.org/10.1002/jbio.202000366>